A cookbook for the investigation of coordination polymers by transition metal K-edge XMCD

Adama N'Diaye,[a] Amélie Bordage,[a*] Lucie Nataf,[b] François Baudelet,[b] Thierry Moreno[b] and Anne Bleuzen[a]

[a]ICMMO, Université Paris Saclay, CNRS, 15 rue Georges Clémenceau, 91405 Orsay, France, and [b]Synchrotron SOLEIL, L'Orme des Merisiers, Saint Aubin, BP 48, 91192 Gif-sur-Yvette, France. *Correspondence e-mail: amelie.bordage@universite-paris-saclay.fr

In order to disentangle the physical effects at the origin of transition metal K-edge X-ray magnetic circular dichroism (XMCD) in coordination polymers and quantify small structural distortions from the intensity of these signals, a systematic investigation of Prussian blue analogs as model compounds is being conducted. Here the effects of the temperature and of the external magnetic field are tackled; none of these external parameters modify the shape of the XMCD signal but they both critically modify its intensity. The optimized experimental conditions, as well as a reliable and robust normalization procedure, could thus be determined for the study of the intrinsic parameters. Through an extended discussion on measurements on other XMCD-dedicated beamlines and for other coordination compounds, we finally provide new transition metal K-edge XMCD users with useful information to initiate and successfully carry out their projects.

1. Introduction

X-ray magnetic circular dichroism (XMCD) has proven to be a rich technique in several fields, using either soft X-rays or hard X-rays (Funk *et al.*, 2005; Nakamura & Suzuki, 2013; van der Laan & Figueroa, 2014; Rogalev & Wilhelm, 2015; Rogalev *et al.*, 2016). The K-edge of transition metals (TMs) lies in the hard X-ray regime, which enables experiments to be performed with demanding sample environments such as diamond anvil cells, for instance to probe magnetism under pressure (Torchio *et al.*, 2014; Baudelet *et al.*, 2016; Itié *et al.*, 2016). Additionally, XMCD retains the chemical sensitivity of X-ray absorption spectroscopy (XAS), which is priceless when two or more TMs are present. Many kinds of compounds could thus be investigated and their properties better understood, for instance oxides (Subías *et al.*, 2009; Ramos *et al.*, 2009), alloys (Dartyge *et al.*, 1995), magnetic multilayers (Pizzini *et al.*, 1995), intermetallic compounds (Boada *et al.*, 2010a), molecular magnets (Train *et al.*, 2004) or Prussian blue analogs (PBAs) (Verdaguer *et al.*, 1995, 1999; Dujardin *et al.*, 1998; Champion *et al.*, 2001; Cafun *et al.*, 2013; Lahiri *et al.*, 2016). All these results were obtained thanks to worldwide-available beamlines allowing for TM K-edge XMCD measurements, using either a scanning setup (Rogalev & Wilhelm, 2015; Haskel *et al.*, 2007; Nakamura & Suzuki, 2013; Poldi *et al.*, 2020)[1] or a dispersive one, for instance on ODE (Baudelet *et al.*, 2011, 2016) at SOLEIL (France), ID24

---
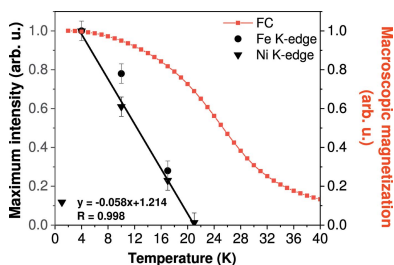
[1] These references are examples of scanning beamlines for XMCD measurements but do not intend to be a complete list.

(Mathon *et al.*, 2004; Pascarelli *et al.*, 2016) at ESRF, EDXAS (Cezar *et al.*, 2010) at LNLS (Brazil), or BL-08 (Patra *et al.*, 2019) at Indus-2 (India). In parallel to these experimental works, several attempts have been made during the last 30 years to understand and disentangle the physical effects originating TM *K*-edge XMCD (Schütz *et al.*, 1987; Ebert *et al.*, 1988; Brouder & Hikam, 1991; Guo, 1998; Bouldi *et al.*, 2017, 2018) but with little success, especially for coordination polymers such as PBAs.

However, TM *K*-edge XMCD has recently appeared as a potentially new tool to quantify small structural distortions in coordination polymers such as PBAs or molecular magnets thanks to Bleuzen and co-workers (Cafun *et al.*, 2013). They demonstrated (i) that significant variations in the XMCD intensity occurred for a piezo-induced structural distortion in a family of model Ni–Fe PBAs, and (ii) that the behaviour of the intensity with pressure was different at the Fe and Ni *K*-edges. This study opened new possibilities to gain novel insights into TM *K*-edge XMCD and also suggested for the first time that the intensity of the XMCD signal could bring new information on PBAs. The previous studies of PBAs by TM *K*-edge XMCD indeed mainly concentrated on the relative sign of the XMCD signal measured at each *K*-edge of the TM contained in the PBA (Verdaguer *et al.*, 1995, 1999; Dujardin *et al.*, 1998; Champion *et al.*, 2001). Therefore we are engaged in a fundamental investigation of TM *K*-edge XMCD in coordination polymers. Our goal is first to disentangle the physical effects involved in these signals and then to establish a new methodology to quantify small structural distortions from the intensity of the TM *K*-edge XMCD signals in order to gain a better understanding of the structure–property relationships in these compounds. To do so, we have developed a completely new experimental approach: a systematic laboratory, TM *K*-edge XMCD and XAS investigation of a series of targeted model compounds. We chose PBAs ($Y_xA_4[B(CN)_6]_{(8+x)/3}·nH_2O$; Y = alkali cation; A, B = 3d transition metals; $x = 0$–4) as model compounds because their isostructurality and chemical versatility enable such series of model compounds to be built. We can indeed independently vary structural and/or electronic parameters, for instance the number of 3d electrons either in the A or B site of the A–NC–B linkage. Such an experimental and chemical approach has never been used to try to (i) understand TM *K*-edge XMCD and (ii) use its intensity to obtain relevant information on the coordination polymers.

However, such investigation of internal effects is worth the effort only if any change in the XMCD intensity can be unambiguously attributed to a change in this internal parameter, without any doubts about the effect of the experimental conditions or data treatment. Bouldi (2017) indeed already observed for metallic Co that the XMCD amplitude (i) is 16% larger with a 2.1 T field than a 1.3 T field, even though the saturating field for Co is 1 T, and (ii) changed by 7% between measurements at 4 K and 300 K, when the Curie temperature is 1393 K at ambient pressure (Lyle, 1954). Such an effect at a temperature much smaller than the Curie temperature turns out to be highly critical in PBAs for which

the very highest observed Curie temperatures are around room temperature for VCr PBAs (Dujardin *et al.*, 1998). So the present paper focuses on preliminary but crucial work performed on two reference PBAs, namely $Ni_4[Fe(CN)_6]_{2.7}$ (hereafter called NiFe) and $Co_4[Fe(CN)_6]_{2.7}$ (hereafter called CoFe): a detailed investigation of the effects of external parameters on the TM *K*-edge XMCD signals of PBAs. Such knowledge, priceless in any XMCD experiments, becomes critical in the investigation of PBA or any other coordination/molecular compounds. A manual normalization procedure had to be developed for our project and completes this work.

All the presented and discussed data were recorded on the dispersive ODE beamline (Baudelet *et al.*, 2011) at Synchrotron SOLEIL (Gif sur Yvette, France). After a presentation of the experimental details in Section 2, we first present in Section 3 TM *K*-edge XMCD on ODE, with a presentation of the general considerations and of an optimized normalization procedure of the data. Next, in Section 4, we detail how we constrained the external parameters (temperature, magnetic field) for our TM *K*-edge XMCD measurements of PBAs; for this investigation, the maximum and integrated intensities of the XMCD signals display the same trends, so only the results for the maximum intensity are shown. Finally, in Section 5, the retained measurement and data treatment procedures are set out; they are further discussed for their extension to measurements on other XMCD-dedicated beamlines and for other coordination compounds, with the aim to provide new TM *K*-edge XMCD users with useful information to initiate and successfully carry out their projects.

2. Experimental details

2.1. Samples

NiFe and CoFe were synthesized by a drop-by-drop addition of a 400 ml aqueous solution of potassium hexacyanoferrate(III) $K_3[Fe(CN)_6]$ ($c = 2.5 \times 10^{-3}$ mol L^{-1}) to a 100 ml aqueous solution of nickel $Ni^{II}(NO_3)_2$ or cobalt $Co^{II}(NO_3)_2$ nitrate ($c = 50 \times 10^{-3}$ mol L^{-1}). The precipitates were washed with distilled water and centrifuged three times, and finally allowed to dry in air at room temperature. The samples were characterized by powder X-ray diffraction at room temperature using the Philips X'Pert diffractometer (Cu $K\alpha_1$ radiation) of the ICMMO instrumentation platform. All diagrams were recorded over the 2θ angle range of 10–70° in steps of 0.01°. An aluminium sample holder was used for all measurements. The cell parameter of NiFe is 10.22 ± 0.02 Å and that of CoFe is 10.31 ± 0.02 Å, which are the expected values for these two PBAs (Cafun *et al.*, 2013; Bleuzen *et al.*, 2008).

2.2. SQUID magnetometry

The macroscopic magnetic properties of NiFe and CoFe were characterized using the Quantum Device XL-7 SQUID magnetometer of the ICMMO instrumentation platform.

5.6 mg of PBA powder was placed in a capsule and 17 mg of eicosane was added to ensure that the particles would not move with the application of the magnetic field. Field-cooled measurements were performed over the 2–100 K temperature range under a 1.3 T magnetic field. The magnetic field dependence of the magnetization up to 4 T was recorded at 4 K.

2.3. TM K-edge XAS on SAMBA

X-ray absorption spectra in the transmission mode were recorded for both PBAs at the Fe/Co/Ni K-edges on the SAMBA beamline (Briois et al., 2011) at SOLEIL (Gif-sur-Yvette, France), which is a conventional scanning beamline. We used a Si(220) monochromator (resolution ∼1 eV) and recorded the spectra in continuous mode. Measurements were performed at room temperature on pellets. Thanks to the use of a defocused beam, no radiation damage was observed. Following the measurements, the spectra were energy-calibrated and conventionally normalized using the ATHENA software (Ravel & Newville, 2005).

3. Transition metal K-edge XMCD on ODE

3.1. General considerations

The ODE beamline (Baudelet et al., 2011) is based on a dispersive setup, installed on a bending magnet at Synchrotron SOLEIL. The description, advantages and drawbacks of dispersive setups can be found elsewhere (Baudelet et al., 1991; Mathon et al., 2004, 2007; Pascarelli & Mathon, 2010; Torchio et al., 2014; Baudelet et al., 2016). All the measurements are performed in transmission. Two polychromators are available: Si(311) and Si(111). The use of the Si(311) enables a resolution improved by a factor of two with respect to the Si(111), but with an energy band above the edge reduced by a factor of two (Baudelet et al., 1991).

The setup of the beamline does not allow the helicity to be changed during measurements and so the XMCD measurements are performed by flipping the applied magnetic field direction, either parallel or anti-parallel to the beam propagation direction (it is achieved by changing the direction of the current in the coils of the electromagnet). The X-ray absorption near-edge structure (XANES) spectrum is derived from the transmitted intensity recorded for one orientation of the magnetic field. The XMCD signal is directly derived from the measured transmitted intensities for each orientation of the magnetic field, and is defined as

$$\text{XMCD} = \mu^+ - \mu^- = \log(I^-/I^+). \qquad (1)$$

In order to work exclusively from the transmitted intensities and be free from possible linear derivation due to beam variations[2], the following sequence of measurements is adopted,

$$I_0^+, I_1^-, I_1^+, I_2^-, I_2^+, \ldots, I_N^-, I_N^+,$$

where N is the number of iterations.[3] The XMCD signal is then defined as

$$\text{XMCD}_N = \frac{1}{2N} \log \frac{I_0^+ (I_1^+)^2 \ldots (I_{N-1}^+)^2 I_N^+}{(I_1^-)^2 \ldots (I_N^-)^2}. \qquad (2)$$

The intensity of the XMCD signal is tightly related to the circular polarization rate of the X-ray beam. Since ODE is installed on a bending magnet, the circular polarization is achieved by selecting out-of-orbit emission from the bending magnet thanks to slits (Baudelet et al., 1991), whose position and size define the circular polarization rate. The circular polarization rate is not experimentally measured on ODE, but a fixed opening of the slits during the whole measurements campaign allows the circular polarization rate to be fixed. This instrumental constraint only implies to measure a given series of samples at all relevant edges during the same beam time, so that the beamline optical setup and consequently the circular polarization rate are fixed. A significant advantage of ODE is indeed that, for a given opening of the slits, the circular polarization rate is constant over the TM K-edge energy range: ±1% variation for the Si(111) polychromator, and ±2% variation for the Si(311) one. With respect to the Si(111) polychromator, the Si(311) polychromator offers a higher stability over the vertical divergence of the beam; a slight change in the slits opening will therefore modify the circular polarization rate to a lesser extent and so the intensity of the XMCD signals. Details are given in Appendix A. Nevertheless, for a more reliable comparison of the XMCD signals measured during different beam times or with data recorded on other beamlines, a key point is to record the XMCD signal of the metallic foil of each investigated edge to renormalize the XMCD intensity.

Regarding the value of the applied magnetic field, it must exceed (i) the coercive field of the studied sample in order to reverse the magnetization (Pizzini et al., 1998) and (ii) the closure point of the hysteresis. When a cryostat is used, the highest magnetic field is 1.3 T, but it can be increased up to 2.1 T for measurements at room temperature; a 7 T magnetic field will also be available soon on ODE. Element-selective magnetization curves can be measured following an appropriate procedure, determined for a given sample from its macroscopic magnetization data.

The cryostat available on ODE was designed for diamond anvil cells (DACs). A DAC can be used as a sample holder for ambient pressure experiments, on condition that no pressure-transmitting medium is used. The main advantage of a DAC is that the parallel surfaces of the diamonds allow for a better homogeneity of the sample. In the TM K-edges range, the diamonds of the DAC may strongly absorb the incoming photons; therefore, one DAC was adapted by replacing the two diamonds with plexiglas plates. All the DACs available on ODE, either with diamonds or plexiglas plates, are made of

---

[2] This was critical for the previous generation of synchrotron facilities, but has become less useful at SOLEIL thanks to the top-up mode which prevents a decrease of the electron beam current.

[3] I_0^+ is here the very first measured transmitted intensity and must not be mistaken with the incoming intensity from the polychromator.

amagnetic materials and optimized for XMCD measurements at low temperatures.

Finally, it must be noted that a damping effect of the white line due to a too thick sample (absorption edge jump above 0.6) can occur. This artefact arises in the particular case of scattering samples measured on a dispersive setup: the intensity of the white line is artificially lowered if the absorption edge jump does not lie in the 0.2–0.5 range. It can be easily avoided by a careful attention to the preparation of the sample.

3.2. Experimental details for the present data

XANES spectra and XMCD signals were recorded for NiFe at the Fe and Ni K-edges, and for CoFe at the Fe and Co K-edges. We used the Si(311) polychromator in order to obtain a high resolution in the white line region of the spectra. Measurements for a variable magnetic field were performed at 4.5 ± 0.5 K using the He-cooled cryostat; it was varied from 0.1 T up to 1.3 T by varying the current within the electromagnet for a fixed gap between the poles. Measurements for a variable temperature were performed at 1.3 T. The XMCD measurements were performed using the procedure described in Section 3.1. Samples were placed in a DAC without pressure-transmitting medium. Attenuators of appropriate thickness were placed before the sample to avoid radiation damage. The XANES spectrum of a metallic foil was recorded at each edge for energy calibration. The data were acquired during the same two-weeks measurements campaign, in order to work with the same settings of the beamline optics and so with a constant circular polarization rate.

3.3. Normalization of the XANES spectra and XMCD signals

3.3.1. Need of a robust procedure. A critical step in the quantification of the small structural distortions in PBAs using the TM K-edge XMCD signals is the normalization of these signals. This normalization is critically dependent on the XANES spectra normalization, as the factor used to set the absorption edge jump to 1 is also used to normalize the intensity of the corresponding XMCD signal.

A strong limitation arising from the use of a dispersive setup to record XAS data can be the available energy range, which depends (i) on the curvature radius of the Si polychromator and (ii) on the investigated edge. In our case, we use the Si(311) polychromator to obtain a high resolution of the XANES spectrum, where most of the XMCD spectral features are observed, and we investigated TM K-edges down to Mn, whose energy (6.539 keV) represents a low-energy limit on ODE. Consequently, the available energy range above the white line extends only up to 60–200 eV depending on the edge. A larger energy range could be obtained by switching to a Si(111) polychromator, but this was not a relevant choice for our project. It must also be noted that, whatever the polychromator, the higher the energy of the edge, the larger the available energy range above the edge. This drawback of a short range above the edge directly impacts the normalization process of the XANES spectra. First, a classical normalization

of the XANES spectrum using the *ATHENA* (or equivalent) software is not always possible: for a too short energy range above the edge (as in our case at the Mn K-edge), the software may not succeed in defining the appropriate post-edge line and consequent background. Then, in the cases when the normalization software mathematically manage to normalize one spectrum, we observed that repetitive normalizations of the same XANES spectrum can all lead to reasonably normalized XANES spectra but with slightly different values of the absorption edge jump used to normalize the spectrum to 1. It may have little effect when considering only the XANES spectra, but it can lead to relatively significant artefacts in the normalized XMCD intensity given the very small intensity of the TM K-edge XMCD signals of PBAs.

Therefore, within the frame of our project, we had to set up a manual XANES and XMCD data treatment procedure based on the use of a long k-range EXAFS spectrum measured on another beamline using a conventional scanning mode. This procedure allowed us to be free from possible artefacts in the XMCD normalized intensity, and so to trustfully compare the signals within model-PBAs series.

3.3.2. Normalization of the XANES spectrum. The first step in this normalization procedure is to obtain a long k-range EXAFS reference spectrum for each compound and edge measured on ODE; here they were obtained by transmission XAS measurements in the conventional scanning mode on the SAMBA beamline. These SAMBA spectra, thanks to measurements up to 800–1000 eV above the edge, could be reliably normalized using *ATHENA* [Figure 1(*a*)]. From this long k-range EXAFS reference spectrum, the ODE spectrum is manually normalized in three steps, illustrated in Figure 1 for the example of CoFe at the Fe K-edge. First, the pre-edge region is set to zero by a simple translation [Figure 1(*b*)]. Then, a baseline is subtracted from the full ODE spectrum; the post-edge region is thus corrected so it becomes parallel to the post-edge region of the SAMBA spectrum [Figure 1(*c*)]. Finally, the ODE spectrum is multiplied by a factor to set the absorption edge jump to 1. The normalization is checked by comparing the ODE and SAMBA spectra [Figure 1(*d*)]: the two of them must superimpose. It is to be noted that the distortion sometimes observed for the ODE spectrum cannot always be corrected enough so that the two spectra superimpose on the whole post-edge energy range measured on ODE; in that case, we concentrate on the region around the white line and multiple-scattering feature, since the main spectral features of the XMCD signals are related to these XANES features.

3.3.3. Normalization of the XMCD signal. The processing of the XMCD signals is done in two steps. First, the XMCD baseline is set to zero. In some cases, a background must be carefully defined and subtracted from the measured XMCD signal, so that the XMCD signal is defined with a flat baseline; strong oscillations due to instabilities between the intensities measured for the two magnetic field directions may indeed be present in the signal (it is to be noted that a homogeneous sample drastically reduces these oscillations). The second step is the normalization itself: the XMCD signal obtained in the
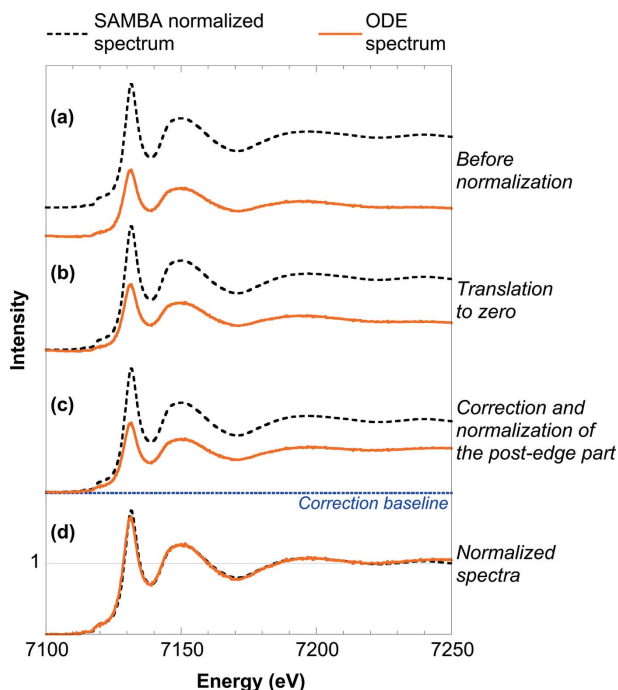
Figure 1
Normalization procedure of the XANES spectrum recorded on ODE in the dispersive setup using the normalized EXAFS spectrum recorded on SAMBA in the conventional scanning mode for the example of CoFe at the Fe *K*-edge. From top to bottom, (*a*) before the normalization of the ODE spectrum, (*b*) pre-edge part adjustment, (*c*) post-edge part normalization, and (*d*) after the full normalization procedure for the ODE spectrum.

first step is multiplied by the factor used to normalize the absorption edge jump of the XANES spectrum to 1.

4. Effect of external parameters on the signal

The XMCD signals presented in this section were normalized using the procedure described in Section 3.3. In addition, for a more direct comparison between the signals at the two edges, and between XMCD and SQUID data, the intensity of the signal at 1.3 T and 4 K was normalized to 1, with a subsequent renormalization of the points at other temperatures/magnetic fields.

4.1. Effect of temperature

To evaluate the impact of the temperature on the signal, Fe and Ni *K*-edge XMCD signals were recorded for NiFe at different temperatures between 4 K and its Curie temperature $T_C = 21$ K (Cafun *et al.*, 2013). The signals recorded at the Fe and Ni *K*-edges are displayed in Figure 2. When increasing the temperature from 4 K, it is noticeable that the shape of the XMCD signals does not change. However, a clear decrease of the intensity as the temperature increases can be observed. These variations were expected, as the ferromagnetic ordering is progressively relaxed as the temperature gets closer to the Curie temperature.

The variation of the maximum intensity at both Fe and Ni *K*-edges for NiFe is displayed in Figure 3, along with the
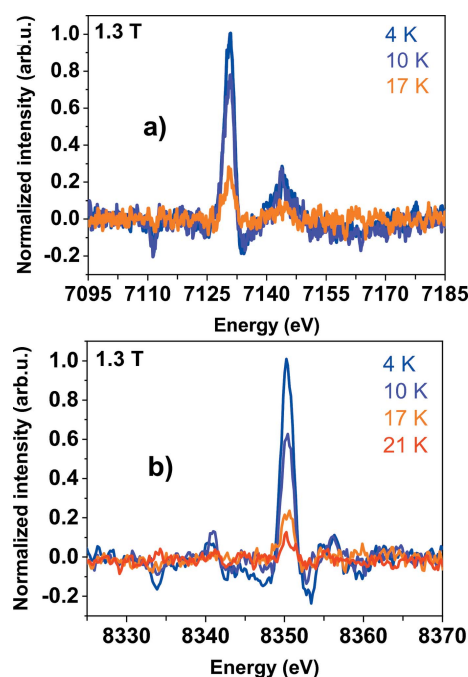
Figure 2
Normalized (*a*) Fe and (*b*) Ni *K*-edge XMCD signals of NiFe recorded at 1.3 T for a variable temperature.

variation of the macroscopic magnetization recorded by SQUID magnetometry also at 1.3 T. First, we can observe that the variation of the XMCD intensity is strictly linear at the Ni *K*-edge and tends to be at the Fe *K*-edge. The different temperature dependences of the XMCD maximum intensities probably reflect different magnetic behaviour of the Ni and Fe sub-lattices. Second, if the intercept of the linear variation of the intensity of the XMCD signal at the Ni *K*-edge with the *x*-axis corresponds well to the magnetic ordering temperature of NiFe, it is interesting to notice that, whatever the edge, the evolution of the XMCD intensity with temperature is different
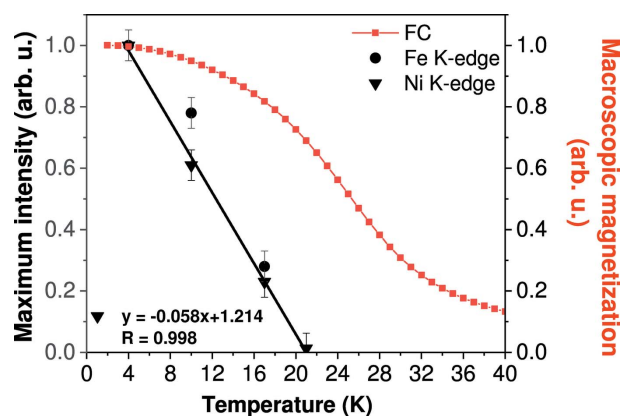
Figure 3
Evolution for NiFe of the maximum intensity of the XMCD signals as a function of temperature at both Fe (circles) and Ni (triangles) *K*-edges along with the macroscopic magnetization recorded by SQUID magnetometry (red curve). All the data were recorded for a 1.3 T magnetic field. The macroscopic magnetization at 4 K (47.4 × 10^3 emu mol^{-1}) was renormalized so that the value is also set to 1.

from the variation of the macroscopic magnetization with temperature. The slope of the curve is steeper for the XMCD signals at both the Ni and Fe K-edges than for the magnetization, which suggests that the intensity of the XMCD signal does not solely and directly reflect the magnetic moment carried by the absorbing atom, as macroscopically measured for the whole sample in a SQUID magnetometer.

Furthermore, Figure 3 shows that (i) at the Ni K-edge, the intensity of the XMCD signals varies by ∼6% per Kelvin, and (ii) at the Fe K-edge, a variation of ∼25% is observed between 4 K and 10 K. This variation of the XMCD intensity with temperature underlines the importance of constraining the temperature to reliably analyze and interpret variations in the XMCD signals intensity in PBAs. Such an important variation of the intensity with temperature can indeed be critical in the study of the effect of intrinsic physical parameters on this intensity for PBAs. For instance, at the Fe K-edge of NiFe, the ∼25% observed here between 4 K and 10 K are of the order of magnitude of the variation observed between 0 and 0.8 GPa by Bleuzen and co-workers (Cafun *et al.*, 2013). It is also not negligible when compared with the ∼40% variation observed at ambient pressure between NiFe and a Cs-containing NiFe PBA ($Cs_1Ni_4[Fe(CN)_6]_3$) (Cafun *et al.*, 2013). Our results on NiFe and the previous work by Bouldi (2017), which revealed a variation of the intensity of 7% between 4 K and room temperature for Co metal (T_C = 1393 K), show that XMCD signals at the TM K-edges are temperature sensitive, whatever the family of compounds. However, as expected, the present results underline that the effect is much more marked for compounds with low Curie temperatures, which is the main case for coordination polymers.

Therefore, the temperature must be very precisely constrained and controlled during the whole experiment. On ODE, the 4.5 ± 0.5 K temperature is reached using a He-cryostat, and higher temperatures are controlled through a heater. Therefore, even if they present the major advantage of a lower He consumption, intermediate temperatures such as 10 K cannot be retained as the measurement temperature for our project, as the heater regulation induces an additional source of artefact due to potential defects in the temperature control.

It must be finally underlined that the effect described here is purely related to the measurements conditions, since all the investigated temperatures lie below the Curie temperature of our PBA. Nevertheless, it is interesting to remember that, for compounds with temperature-dependent ordered magnetic states, XMCD measurements at different temperatures can also bring valuable information on the different states and on the transition between them (Chaboy *et al.*, 1998; Bartolomé *et al.*, 2005; Laguna-Marco *et al.*, 2009; Carvallo *et al.*, 2010; Boada *et al.*, 2010b; Alonso *et al.*, 2012).

4.2. Effect of magnetic field

Another critical parameter in an XMCD experiment is the value of the external magnetic field. Most often, this value is fixed above the saturation magnetization of the sample to
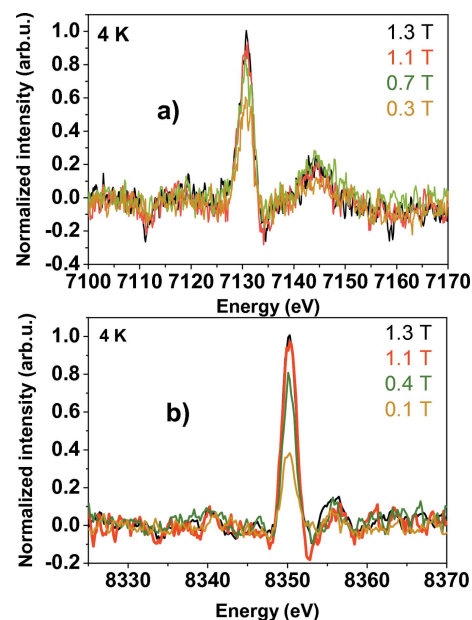

Figure 4
Normalized (*a*) Fe and (*b*) Ni K-edge XMCD signals of NiFe recorded at 4 K for a decreasing variable magnetic field.

avoid any artefact from the magnetic field. Nevertheless, in some cases, an external magnetic field higher than the saturation magnetization still influences the intensity of the XMCD signal, as observed for instance in the case of Co metal (Bouldi, 2017). In PBAs, this question is even more critical as the magnetization of some of them tends to a saturation value but never completely reaches it. Therefore, reaching magnetization saturation is not realistic for all compounds. In order to evaluate the effect of the external magnetic field, we recorded the XMCD signals for an increasing or a decreasing magnetic field between 0.1 T and 1.3 T (maximum value currently reachable by ODE's electromagnet) for CoFe and NiFe at both edges.

Both PBAs display the same behaviour with magnetic field, so only the signals of NiFe at the Fe and Ni K-edges are shown in Figures 4(*a*) and 4(*b*) for the case of a decreasing magnetic field. As for the temperature, this external parameter does not modify the number of spectral features and the shape of the XMCD signals, whatever the investigated PBA (NiFe or CoFe), the edge (Fe or Ni/Co K-edge) or the way to reach the magnetic field value.

But a modification of the external magnetic field value significantly changes the intensity of the signal. The variation of the maximum intensity of the XMCD signals of NiFe at both edges is plotted in Figure 5 along with the macroscopic magnetization recorded by SQUID magnetometry; all the data were normalized to 1 at 1.3 T for a more direct comparison. It is interesting to notice first that the evolution of the intensity displays a similar behaviour for both an increasing and decreasing magnetic field and also whatever the investigated edge. This variation of the intensity follows the trend of the macroscopic magnetization, with a strong increase of the intensity for low values of the magnetic field
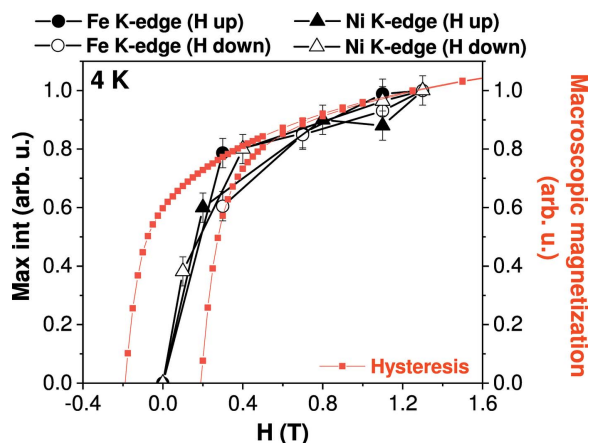
Figure 5
Evolution for NiFe of the maximum intensity of the XMCD signals as a function of the applied external magnetic field for Fe (circle symbols) and Ni (triangle symbols) for an increasing (black symbols) and decreasing (white symbols) magnetic field, compared with the macroscopic magnetization recorded by SQUID magnetometry (red line). The macroscopic magnetization at 1.3 T (47.4×10^3 emu mol^{-1}) was renormalized so that the value is also set to 1.

followed by a slow increase over the 0.5–1.3 T magnetic field range out of the hysteresis loop. Like magnetization, the intensity of the XMCD signals does not reach a plateau. So TM *K*-edge XMCD reflects the macroscopic magnetic behaviour of the PBAs despite it probes the 4*p* orbitals, which present a magnetic character only through the hybridization with and/or polarization from the magnetic 3*d* orbitals.

So magnetic field, as temperature, is a critical parameter in our XMCD experiments on PBAs and so must be very precisely constrained. Since reaching magnetization saturation is not realistic for our PBAs, all the experiments must be performed at the highest available magnetic field, 1.3 T on ODE when a cryostat must be used. It is to be noted that, whatever the PBA, 1.3 T enables to be both above the closure point of the hysteresis loop and above the coercive field so that the magnetization can be reversed without artefact (Pizzini *et al.*, 1998).

As for temperature, the effect related to the different values of the magnetic field described here is purely related to the measurements conditions, since all the measurements are performed below the Curie temperature and so in the same magnetic ordering state. Nevertheless, it is interesting to point out that XMCD measurements at different magnetic field can also bring valuable information on the investigated compound (Train *et al.*, 2004; Bartolomé *et al.*, 2005; Osawa *et al.*, 2007; Boada *et al.*, 2010*b*; Chaboy *et al.*, 2010; Guglieri *et al.*, 2012; Koumousi, 2015; Jafri, 2016; Lahiri *et al.*, 2016; Platunov *et al.*, 2019; Pajerowski *et al.*, 2020). Finally, our goal here was to optimize the value of the applied magnetic field for our PBAs but not to perform element-selective magnetic hysteresis from XMCD; these measurements require either the direction of the magnetic field to be fixed and the helicity of the photons switched (Pizzini *et al.*, 1997), or to apply an appropriate procedure if the helicity cannot be switched.

5. Discussion

5.1. Retained measurements and data treatment procedures for TM *K*-edge XMCD of PBAs on ODE

The results presented in Section 4 clearly demonstrate the high sensitivity of the XMCD intensity to external parameters in the case of PBAs. Since our goals are to disentangle the physical effects originating TM *K*-edge XMCD and quantify small structural distortions from variations in the XMCD intensity, we must ensure that no artefact arises from these external factors in the study of model-compounds series. Our present results enable a measurement procedure to be defined for all our TM *K*-edge XMCD measurements of PBAs on ODE:

(i) For a given series of samples, the measurements at all relevant edges must be performed during the same campaign without changes in the beamline optical setup.

(ii) The sample must be thin enough so that the absorption edge jump lies within the 0.2–0.5 range.

(iii) Measurements must be performed at 4.5 ± 0.5 K.

(iv) For the magnetic field, defined by the gap between the electromagnet poles, this gap must be (i) calibrated and carefully respected using a gauge and (ii) the smallest possible in order to obtain the highest possible magnetic field (1.3 T here because of the cryostat). For our investigated PBAs, measurements at 1.3 T also ensure that the applied magnetic field is much higher than the coercive field (here, $H_C = 0.2$ T for NiFe and 0.12 T for CoFe) and also than the closure field of the magnetization hysteresis.

With regard to the data treatment, for our TM *K*-edge measurements on ODE performed using the Si(311) polychromator, a two-step process is necessary: (i) exact normalization of the XANES spectra using the long *k*-range EXAFS spectrum recorded in the conventional scanning mode as a reference, and then (ii) normalization of the XMCD signal. The retained manual procedure for our project to trustfully compare the XMCD signals recorded for different samples is:

(i) Each sample measured on ODE must be measured in the conventional scanning mode on another XAS beamline, here the SAMBA beamline at SOLEIL.

(ii) The X-ray absorption spectrum measured using the conventional scanning mode must be conventionally normalized using *ATHENA* or a similar software.

(iii) The XANES spectrum recorded on ODE is manually normalized using the spectrum measured in the conventional scanning mode as a reference.

(iv) The XMCD signal baseline is set flat and to zero, and the signal normalized using the factor defined to set the edge jump of the XANES spectrum to 1.

Figure 6 shows that, if these experimental conditions are fulfilled and the data treatment procedure applied, the XMCD signal measured for two different DAC loads superimposes, which demonstrates that (i) a control of the external parameters and (ii) an optimized data treatment enable a reproducible set of data.
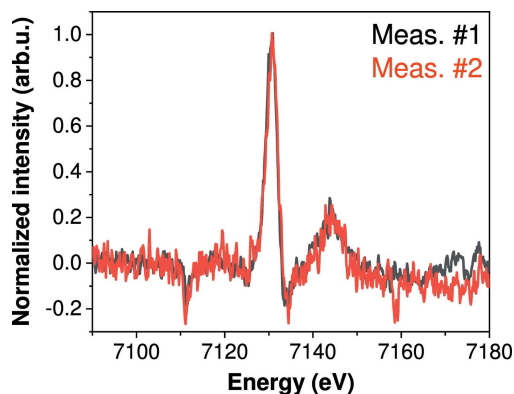
Figure 6
Fe K-edge XMCD signals of NiFe recorded in the exact same experimental conditions (4 K, 1.3 T) for two different DAC loads and normalized using our manual procedure.

5.2. Key points for TM K-edge XMCD measurements of other coordination polymers

These measurements and data treatment procedures were optimized for our project based on PBA and TM K-edge experiments on the ODE beamline. But they can be adapted and extrapolated to the study of any other coordination polymers on another XMCD-dedicated beamline, on condition of keeping in mind some key points that we detail now.

(1) The constraints related to the experimental conditions (temperature, external magnetic field, type of setup and detection mode, circular polarization rate ...) impose to complete a whole study on the same beamline to minimize the number of possible artefacts.

(2) Since the main feature in the TM K-edge XMCD signal corresponds to the white line of the XANES spectrum, careful attention must be given to avoid any artefact in the white line region. For experiments on a dispersive setup, this implies optimizing the thickness of the sample to avoid the damping effect of the white line. For experiments on a beamline based on the conventional scanning mode and with measurements in the total fluorescence yield detection mode, measurements must be free from self-absorption effects or carefully corrected (Goulon *et al.*, 1982; Rogalev & Wilhelm, 2015).

(3) The measurements of a series of samples must be performed at the same and lowest possible temperature.

(4) The measurements of a series of samples must be performed at the same and highest possible magnetic field. An important point if the setup does not allow the helicity inversion is to have a magnetic field much higher than the coercive field of the samples (Pizzini *et al.*, 1998) and, if the macroscopic magnetization presents a hysteresis, above its closure point.

(5) To perform an element-selective magnetization curve from XMCD, either the magnetic field direction is fixed and the helicity switched (Pizzini *et al.*, 1997), or an appropriate procedure must be implemented.

(6) The circular polarization rate must be measured or/and the XMCD of metallic foil recorded as a reference.

(7) For favourable cases, a classical normalization with already existing softwares can lead to robustly normalized data. But, if needed, a manual normalization procedure must be optimized (this work; Bouldi, 2017). A key point is to carefully apply the same normalization procedure to all samples.

(8) For measurements performed using a dispersive setup, in the unfavourable cases of a short range above the edge (either because of the polychromator or/and the edge energy), one of the critical points for the data treatment is to have a reference long k-range EXAFS spectrum to reliably normalize the dispersive XANES spectrum, whatever the chosen normalization procedure (with an already existing software or a manual procedure). It must be noted that a combination of measurements from a dispersive setup and a conventional scanning beamline can also bring valuable complementary information on the sample (Pascarelli *et al.*, 2016), independently from being used as a reference for the normalization.

(9) If both the magnetic field and the helicity of the X-ray beam can be changed, the following measurements procedure may help to further reduce systematic errors in the XMCD signal. The helicity is fixed for the left circular polarization, and the XMCD is acquired for each magnetic field direction. The helicity is then switched to the right circular polarization and the XMCD is acquired again for each magnetic field direction. The final XMCD signal is the average of these two signals (Mathon *et al.*, 2004).

(10) For measurements at other edges, details about experimental aspects and data analyses can be found in papers by Rogalev and co-authors for the tender and hard X-ray range (Rogalev & Wilhelm, 2015; Rogalev *et al.*, 2016), and by van der Laan and Figueroa for the soft X-ray range (van der Laan & Figueroa, 2014).

6. Conclusion

To conclude, all the results presented here demonstrate the importance of constraining the external parameters to trustfully study the effects of intrinsic parameters. For our project dedicated to PBAs and undertaken on the ODE beamline, we could thus set up the appropriate measurement conditions for TM K-edge XMCD signals of PBAs: measurements must be performed at strictly 4.5 ± 0.5 K and 1.3 T (defined through a calibrated gap of the electromagnet), and with the same beamline optics setup during the whole beam time. We also presented an optimized manual procedure for the treatment of our data.

As an example, we already successfully applied these measurement and normalization procedures to study a series of bimetallic $A_4[Fe(CN)_6]_{2.7}$ PBAs, in which A is varied ($A =$ Mn, Co, Ni, Cu), in order to evaluate the effect of a change in the number of $3d$ electrons at the A site of the PBA on the TM K-edge XMCD signal. Thanks to these procedures, the variation of the intensity of the XMCD signal could be unambiguously assigned to the variation of the physical parameter that has been varied along the series of compounds, clearly showing a correlation between the total spin of the

absorbing atom and the XMCD signal (N'Diaye *et al.*, unpublished). Further work on other relevant model series is also in progress. Combined, these results will enable to fully disentangle the physical effects that originate these signals in coordination polymers and hence open TM *K*-edge XMCD to new studies.

APPENDIX *A*
Evolution of the circular polarization rate on ODE

The circular polarization rate on ODE has been determined at the position of the sample. Figure 7 displays this circular polarization rate over the 0.5–0.7 mrad range of the vertical divergence of the beam for the TM *K*-edge range (7–9 keV) and at 15 keV for each polychromator. Figure 7(*a*), which shows the results for the Si(111) polychromator, clearly demonstrates that, for a given vertical divergence, the change of energy over this range does not impact the circular polarization rate, with only ±1% variation between 7 and 15 keV. This means that, as long as the slits opening, and thus the vertical divergence, do not change, the circular polarization rate is constant, and so the intensity of the XMCD signal recorded at different TM *K*-edges can be compared. Nevertheless, if the opening of the slits, and thus the divergence, is modified, the circular polarization rate also changed; this underlines that reference XMCD signals must be recorded to compare data acquired during different beam times. The case of the Si(311) polychromator is shown in Figure 7(*b*). In the TM *K*-edge energy range, the variations of the circular polarization rate are slightly higher than with the Si(111) polychromator (4% between 7 and 9 keV), but are still small enough to be considered negligible and with no significant effect on the XMCD signal intensity. But, contrary to the Si(111) polychromator, the Si(311) offers a more stable circular polarization rate over vertical divergence, meaning that slight changes in the slits opening will almost not affect the circular polarization rate.

Figure 7
Calculated circular polarization rate at the sample position for the 7–9 keV energy range (TM *K*-edges) and at 15 keV in the case of (*a*) the Si(111) polychromator and (*b*) the Si(311) polychromator.

References

Alonso, J., Fdez-Gubieda, M. L., Sarmiento, G., Chaboy, J., Boada, R., García Prieto, A., Haskel, D., Laguna-Marco, M. A., Lang, J. C., Meneghini, C., Fernández Barquín, L., Neisius, T. & Orue, I. (2012). *Nanotechnology*, **23**, 025705.

Bartolomé, F., Herrero-Albillos, J., García, L., Bartolomé, J., Jaouen, N. & Rogalev, A. (2005). *J. Appl. Phys.* **97**, 10A503.

Baudelet, F., Dartyge, E., Fontaine, A., Brouder, C., Krill, G., Kappler, J.-P. & Piecuch, M. (1991). *Phys. Rev. B*, **43**, 5857–5866.

Baudelet, F., Kong, Q., Nataf, L., Cafun, J.-D., Congeduti, A., Monza, A., Chagnot, S. & Itié, J.-P. (2011). *High. Press. Res.* **31**, 136–139.

Baudelet, F., Nataf, L. & Torchio, R. (2016). *High. Press. Res.* **36**, 429–444.

Bleuzen, A., Cafun, J.-D., Bachschmidt, A., Verdaguer, M., Münsch, P., Baudelet, F. & Itié, J.-P. (2008). *J. Phys. Chem. C*, **112**, 17709–17715.

Boada, R., Piquer, C., Laguna-Marco, M. & Chaboy, J. (2010*a*). *Phys. Rev. B*, **81**, 100404.

Boada, R., Piquer, C., Laguna-Marco, M. & Chaboy, J. (2010*b*). *Phys. Rev. B*, **82**, 052407.

Bouldi, N. (2017). *Theory of X-ray circular dichroism and application to materials under pressure.* PhD thesis, Sorbonne Université, France.

Bouldi, N., Sainctavit, P., Juhin, A., Nataf, L. & Baudelet, F. (2018). *Phys. Rev. B*, **98**, 064430.

Bouldi, N., Vollmers, N., Delpy-Laplanche, C., Joly, Y., Juhin, A., Sainctavit, P., Brouder, C., Calandra, M., Paulatto, L., Mauri, F. & Gerstmann, U. (2017). *Phys. Rev. B*, **96**, 085123.

Briois, V., Fonda, E., Belin, S., Barthe, L., La Fontaine, C., Langlois, F., Ribbens, M. & Villain, F. (2011). *UVX 2010*, pp. 41–47.

Brouder, C. & Hikam, M. (1991). *Phys. Rev. B*, **43**, 3809–3820.

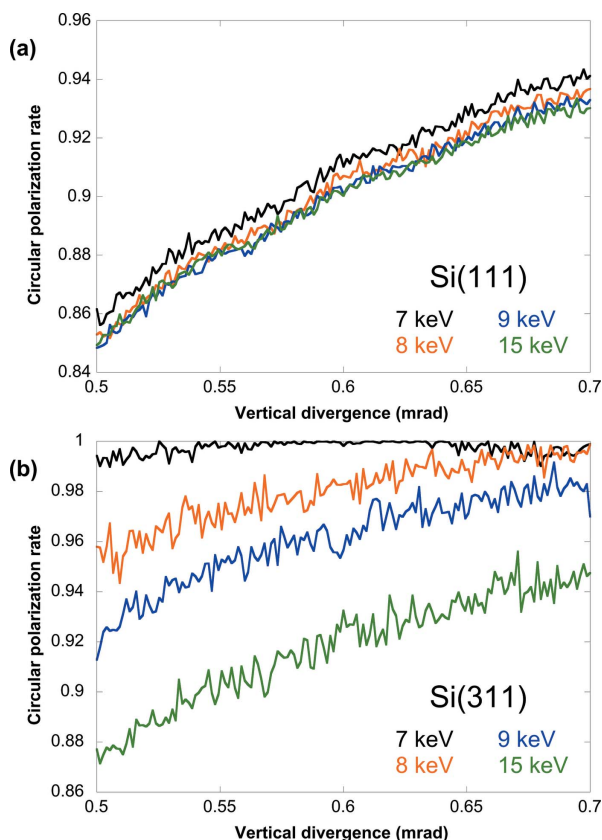Cafun, J.-D., Lejeune, J., Itié, J.-P., Baudelet, F. & Bleuzen, A. (2013). *J. Phys. Chem. C*, **117**, 19645–19655.

research papers

Carvallo, C., Sainctavit, P., Arrio, M.-A., Guyodo, Y., Penn, R. L., Forsberg, B., Rogalev, A., Wilhelm, F. & Smekhova, A. (2010). *Geophys. Res. Lett.* **37**, L11306.

Cezar, J. C., Souza-Neto, N. M., Piamonteze, C., Tamura, E., Garcia, F., Carvalho, E. J., Neueschwander, R. T., Ramos, A. Y., Tolentino, H. C. N., Caneiro, A., Massa, N. E., Martinez-Lope, M. J., Alonso, J. A. & Itié, J.-P. (2010). *J. Synchrotron Rad.* **17**, 93–102.

Chaboy, J., Boada, R., Piquer, C., Laguna-Marco, M., García-Hernández, M., Carmona, N., Llopis, J., Ruíz-González, M., González-Calbet, J., Fernández, J. & García, M. A. (2010). *Phys. Rev. B*, **82**, 064411.

Chaboy, J., García, L. M., Bartolomé, F., Marcelli, A., Cibin, G., Maruyama, H., Pizzini, S., Rogalev, A., Goedkoop, J. & Goulon, J. (1998). *Phys. Rev. B*, **57**, 8424–8429.

Champion, G., Escax, V., Cartier dit Moulin, C., Bleuzen, A., Villain, F., Baudelet, F., Dartyge, E. & Verdaguer, M. (2001). *J. Am. Chem. Soc.* **123**, 12544–12546.

Dartyge, E., Baudelet, F., Brouder, C., Fontaine, A., Giorgetti, C., Kappler, J.-P., Krill, G., Lopez, M. & Pizzini, S. (1995). *Physica B*, **208–209**, 751–754.

Dujardin, E., Ferlay, S., Phan, X., Desplanches, C., Cartier dit Moulin, C., Sainctavit, P., Baudelet, F., Dartyge, E., Veillet, P. & Verdaguer, M. (1998). *J. Am. Chem. Soc.* **120**, 11347–11352.

Ebert, H., Strange, P. & Gyorffy, B. (1988). *J. Appl. Phys.* **63**, 3055–3057.

Funk, T., Deb, A., George, S. J., Wang, H. & Cramer, S. P. (2005). *Coord. Chem. Rev.* **249**, 3–30.

Goulon, J., Goulon-Ginet, C., Cortes, R. & Dubois, J. (1982). *J. Phys. Fr.* **43**, 539–548.

Guglieri, C., Laguna-Marco, M., García, M., Carmona, N., Céspedes, E., García-Hernández, M., Espinosa, A. & Chaboy, J. (2012). *J. Phys. Chem. C*, **116**, 6608–6614.

Guo, G. (1998). *Phys. Rev. B*, **57**, 10295–10298.

Haskel, D., Tseng, Y., Lang, J. & Sinogeikin, S. (2007). *Rev. Sci. Instrum.* **78**, 083904.

Itié, J.-P., Baudelet, F. & Rueff, J.-P. (2016). *X-ray Absorption and X-ray Emission Spectroscopy – Theory and Applications*, Vol. II, edited by J. A. van Bokhoven & C. Lamberti, pp. 385–405. Wiley.

Jafri, S. F. (2016). *Photomagnetic cobalt ferrycianide Prussian Blue analogues probed by X-ray magnetic circular dichroism (XMCD)*. PhD thesis, Université Pierre et Marie Curie, France.

Koumousi, E. S. (2015). *Synthesis and characterization of dinuclear [Fe(μ-CN)Co] complexes exhibiting metal-to-metal electron transfer properties*. PhD thesis, Universitéde Bordeaux, France.

Laan, G. van der & Figueroa, A. I. (2014). *Coord. Chem. Rev.* **277–278**, 95–129.

Laguna-Marco, M. A., Piquer, C. & Chaboy, J. (2009). *Phys. Rev. B*, **80**, 144419.

Lahiri, D., Choi, Y., Yusuf, M., Kumar, A., Ramanan, N., Chattopadhyay, S., Haskel, D. & Sharma, S. M. (2016). *Mater. Res. Expr.* **3**, 036101.

Lyle, P. (1954). *Phys. Rev.* **93**, 384–392.

Mathon, O., Baudelet, F., Itié, J.-P., Pasternak, S., Polian, A. & Pascarelli, S. (2004). *J. Synchrotron Rad.* **11**, 423–427.

Mathon, O., van der Linden, P., Neisius, T., Sikora, M., Michalik, J. M., Ponchut, C., De Teresa, J. M. & Pascarelli, S. (2007). *J. Synchrotron Rad.* **14**, 409–415.

Nakamura, T. & Suzuki, M. (2013). *J. Phys. Soc. Jpn*, **82**, 021006.

N'Diaye, A., Bordage, A., Nataf, L., Baudelet, F., Rivière, E. & Bleuzen, A. (Unpublished). https://hal.archives-ouvertes.fr/hal-03155441.

Osawa, H., Kawamura, N., Matsuda, T., Arimoto, Y., Tokoro, H., Hashimoto, K. & Ohkoshi, S.-I. (2007). *AIP Conf. Proc.* **882**, 526–528.

Pajerowski, D., Escanhoela, C. Jr, Haskel, D., Prisk, T., Frontzek, M., Phelan, D., Mihalik, M. Jr & Mihalik, M. (2020). *J. Magn. Magn. Mater.* **497**, 165968.

Pascarelli, S. & Mathon, O. (2010). *Phys. Chem. Chem. Phys.* **12**, 5535–5546.

Pascarelli, S., Mathon, O., Mairs, T., Kantor, I., Agostini, G., Strohm, C., Pasternak, S., Perrin, F., Berruyer, G., Chappelet, P., Clavel, C. & Dominguez, M. C. (2016). *J. Synchrotron Rad.* **23**, 353–368.

Patra, N., Sachan, U. G. P. S., SundarRajan, S., Malhotra, S., Harad, V., Agarwal, A., Divedi, A., Jha, S. N. & Bhattacharyya, D. (2019). *J. Synchrotron Rad.* **26**, 445–449.

Pizzini, S., Bonfim, M., Baudelet, F., Tolentino, H., San Miguel, A., Mackay, K., Malgrange, C., Hagelstein, M. & Fontaine, A. (1998). *J. Synchrotron Rad.* **5**, 1298–1303.

Pizzini, S., Fontaine, A., Garcia, L., Bobo, J.-F., Piecuch, M., Baudelet, F., Malgrange, C., Alimoussa, A., Snoeck, E. & Casanove, M. (1997). *J. Magn. Magn. Mater.* **166**, 38–44.

Pizzini, S., Fontaine, A., Giorgetti, C., Dartyge, E. J.-F. B., Bobo, J. F., Piecuch, M. & Baudelet, F. (1995). *Phys. Rev. Lett.* **74**, 1470–1473.

Platunov, M., Kazak, N., Dudnikov, V., Temerov, V., Gudim, I., Knyazev, Y., Gavrilkin, S., Dyadkin, V., Dovgaliuk, I., Chernyshov, D., Hen, A., Wilhelm, F., Rogalev, A. & Ovchinnikov, S. (2019). *J. Magn. Magn. Mater.* **479**, 312–316.

Poldi, E. H. T., Escanhoela Jr, C. A., Fonseca Jr, J., Eleotério, M. A. S., dos Reis, R. D., Lang, J. C., Haskel, D. & Souza-Neto, N. M. (2020). *J. Synchrotron Rad.* **27**, 1240–1246.

Ramos, A., Tolentino, H., Soares, M., Grenier, S., Bunău, O., Joly, Y., Baudelet, F., Wilhelm, F., Rogalev, A., Souza, R., Souza-Neto, N., Proux, O., Testemale, D. & Caneiro, A. (2009). *J. Phys. Conf. Ser.* **190**, 0120896.

Ravel, B. & Newville, M. (2005). *J. Synchrotron Rad.* **12**, 537–541.

Rogalev, A., Ollefs, K. & Wilhelm, F. (2016). *X-ray Absorption and X-ray Emission Spectroscopy – Theory and Applications*, Vol. II, edited by J. A. van Bokhoven & C. Lamberti, pp. 671–694. Wiley.

Rogalev, A. & Wilhelm, F. (2015). *Phys. Metals Metallogr.* **116**, 1285–1336.

Schütz, G., Wagner, W., Wilhelm, W., Kienle, P., Zeller, R., Frahm, R. & Materlik, G. (1987). *Phys. Rev. Lett.* **58**, 737–740.

Subías, G., Cuartero, V., García, J., Blasco, J., Mathon, O. & Pascarelli, S. (2009). *J. Phys. Conf. Ser.* **190**, 012089.

Torchio, R., Mathon, O. & Pascarelli, S. (2014). *Coord. Chem. Rev.* **277–278**, 80–94.

Train, C., Baudelet, F. & Cartier dit Moulin, C. (2004). *J. Phys. Chem. B*, **108**, 12413–12417.

Verdaguer, M., Bleuzen, A., Marvaud, V., Vaissermann, J., Seuleiman, M., Desplanches, C., Scuiller, A., Train, C., Garde, R., Gelly, G., Lomenech, C., Rosenman, I., Veillet, P., Cartier, C. & Villain, F. (1999). *Coord. Chem. Rev.* **190–192**, 1023–1047.

Verdaguer, M., Mallah, T., Hélary, C., L'Hermite, F., Sainctavit, P., Arrio, M. A., Babel, D., Baudelet, F., Dartyge, E. & Fontaine, A. (1995). *Physica B*, **208–209**, 765–767.